Published in final edited form as:
Comput Biol Med. 2011 September ; 41(9): 780–789. doi:10.1016/j.compbiomed.2011.06.014.

Segmentation of the Central-Chest Lymph Nodes in 3D MDCT Images

Kongkuo Lu and **William E. Higgins***
Dept. of Electrical Engineering, Penn State University, University Park, PA 16802 USA

Abstract

Central-chest lymph nodes play a vital role in lung-cancer staging. The definition of lymph nodes from three-dimensional (3D) multidetector computed-tomography (MDCT) images, however, remains an open problem. We propose two methods for computer-based segmentation of the central-chest lymph nodes from a 3D MDCT scan: the single-section live wire and the single-click live wire. For the single-section live wire, the user first applies the standard live wire to a single two-dimensional (2D) section after which automated analysis completes the segmentation process. The single-click live wire is similar but is almost completely automatic. Ground-truth studies involving human 3D MDCT scans demonstrate the robustness, efficiency, and intra-observer and inter-observer reproducibility of the methods.

Keywords

lymph node; 3D imaging; thoracic imaging; lung cancer; MDCT; image segmentation; live wire

1 Introduction

The central-chest lymph nodes play a vital role in lung-cancer staging [1–3]. The standard lymph-node staging procedure involves identification of suspect lymph nodes in a chest CT scan followed by bronchoscopic nodal sampling. Modern MDCT scanners provide detailed high-resolution 3D images of the anatomy [4, 5]. Even though MDCT has become a standard tool for lung-cancer staging, partial-volume effects and limited dynamic range in discriminating different soft tissues make it difficult to define soft-tissue structures in a 3D MDCT image. In particular, the definition of lymph nodes proves especially difficult, because lymph nodes vary greatly in size, shape, and gray-scale consistency. They also often have undiscernible boundaries with surrounding soft-tissue structures such as airways and vessels (Figure 1). We propose two methods for computer-based segmentation of the central-chest lymph nodes in a 3D MDCT scan.

Regarding past efforts at devising computer-based methods for defining lymph nodes in CT chest images, Vining *et al.* relied on manual image “painting” of individual 2D MDCT sections to define 3D lymph nodes, as did McAdams *et al.* [6,7]. Honea *et al.* proposed 2D

*Corresponding author. Fax: 1-814-863-5341. weh2@psu.edu.

Conflict of Interest Statement Neither Kongkuo Lu or William E. Higgins have a conflict of interest to disclose in relation to the work described in this paper.

and 3D methods for lymph-node segmentation based on active contour models, but they only evaluated their methods on synthetic images and did not consider realistic situations [8, 9]. Yan *et al.* presented an edge-based matching method, but gave no evaluation results [10]. Kiraly *et al.* presented a method for labeling preidentified and presegmented central-chest lymph nodes, but did not offer a segmentation method [11]. Feuerstein *et al.* proposed an automatic method for detecting candidate lymph nodes, but did not put forth a follow-on method for segmenting the detected candidates [12]. Finally, researchers have considered lymph-node segmentation in other domains, such as the abdomen, pelvis, and neck, but it is unclear if these methods could be applicable to the chest and 3D MDCT and they again sometimes require human interaction [13, 14]. Thus, central-chest lymph-node segmentation from 3D MDCT images remains an open problem.

Our two methods are motivated by the general paradigm of active contour analysis and draw upon the recently proposed notion referred to as the *live wire* [15–19]. For the first method, referred to as the single-section live wire, the user first applies the standard 2D live wire to a single 2D section of a given 3D MDCT image, after which automated analysis completes the segmentation process. The second method, referred to as the single-click live wire, is very similar to the single-section method but is almost completely automatic. The methods constitute part of a general Lymph-Node Station Mapper System (LNSM) we have been devising for nodal station analysis and procedure planning [20–22]. The methods have also been used extensively in our efforts for the planning and follow-on guidance of lung-cancer assessment procedures [23–25]. Section 2 describes the methods in detail, Section 3 presents experimental results, and Section 4 offers concluding remarks.

2 METHODS

Given an input 3D MDCT image I, the goal is to arrive at a 3D segmentation B of a lymph node of interest. For both the single-section and single-click live-wire methods, the user provides some form of initialization information on a selected 2D reference section I_r. Automated analysis then completes the segmentation of B on the remaining 2D sections of I ($i < r$ and $i > r$).

2.1 Overview of the 2D Live Wire

Before proceeding, we first overview the live wire, which is central to both methods. The live wire has become well established as a robust rapid means for defining accurate boundaries of arbitrary regions [15–19]. A user interactively guides the boundary-definition process by moving the computer mouse along a region's boundary, while a free-running automatic background process (the “live wire”) computes a suggested boundary. In this way, not only can a boundary be rapidly computed, but the user can guide the process over problematic portions exhibiting weak or uncertain boundaries.

The live wire casts the boundary-detection problem as an optimal graph search via local active contour analysis. To begin the process on 2D section I_r, the user selects a starting seed pixel s_1 roughly situated on the desired boundary B_r and then hovers the mouse over a succeeding candidate seed s_2 (Figure 2). The live wire then employs Dijkstra's graph-search algorithm and the cost function

$$l(p,q) = w_G f_g(q) + w_Z f_Z(q) + w_{d_1} f_{D_1}(p,q) + w_{D_2} f_{D_2}(p,q) \quad (1)$$

to interactively suggest a locally optimal path between all 8-connected pairs of pixels (p, q) between s_1 and s_2 and contained within a prespecified working area [15,16,18,26]. If the user is satisfied with the suggested path, he/she clicks on s_2 to keep this result and then

moves the mouse to the next candidate seed s_3. This process continues until the desired closed boundary contour B_r, having aggregate cost

$$\bar{c} = \sum_{(p,q)\in B_r} l(p,q), \tag{2}$$

is defined, where (2) accumulates the costs $l(p, q)$ of all successive connected pairs (p, q) along the complete boundary B_r. In (1), $l(p, q)$ defines the local cost between pixel pair (p, q), $f_Z(q)$, $f_G(q)$, $f_D1(p, q)$, and $f_{D2}(p, q)$ are cost components depending on image gradient and gradient-direction features, and w_G, w_Z, w_{D1} and w_{D2} are user-specified weights. Please refer to [18] for complete detail on the 2D live-wire algorithm and cost function (1).

A fundamental assumption made by both of our 3D segmentation methods is that the boundary of B changes little between successive 2D sections of I; i.e.,

$$B_i \approx B_{i+1} \tag{3}$$

where $B_i \subset I_i$ and $B_{i+1} \subset I_{i+1}$. Relation (3) is a reasonable assumption for MDCT-based chest image analysis, since target lymph nodes typically have dimensions > 10 mm (e.g., Figure 1), while the 3D MDCT chest images we consider have 2D section spacing $\Delta z = 0.5$ mm and transverse-plane sampling intervals $\Delta x = \Delta y < 1.0$ mm (Section 3). Sections 2.2 and 2.3 describe our proposed methods, and Section 2.4 discusses miscellaneous issues.

2.2 Single-Section Live Wire

Figure 3 schematically illustrates the flow of the single-section live-wire method. Basically, the user first selects a suitable reference 2D section $I_r \subset I$ and then defines B_r, the lymph node's boundary on I_r, using the standard 2D live wire. Next, initialized by the results for I_r, automatic analysis completes the 3D segmentation of lymph node B for the remaining 2D sections of I. Per Figure 3 and the example of Figure 4, the complete method is the following:

1. User Interaction:
   - **(a)** The user interactively scrolls through 2D sections of I in the vicinity of lymph node B and selects a section I_r approximately central to B's volume.
   - **(b)** The user draws a rectangular working area, which loosely bounds B, and then runs the interactive 2D live-wire process on I_r to define 2D reference boundary B_r (Figure 4ab).
2. Automatic Analysis:
   - **(a)** Begin processing sections I_i, $i > r$, by letting $i = r + 1$.
   - **(b)** Project the reference boundary B_r onto I_i. Create the list

$$\mathcal{L} = \left\{ p_1, p_2, \cdots, p_{N_{B_r}} \right\} \tag{4}$$

consisting of the pixels $p_j \in B_r$ ordered sequentially, where N_{Br} denotes the number of pixels constituting B_r.

(c) Initialize the intermediate boundary cost $\bar{c}$ for B_i to a large value, where B_i denotes B's 2D boundary on I_i. Also, in preparation for the automatic live-wire process of step (d), form an initial seed set S_i for B_i by selecting M evenly spaced pixels $p_j \in \mathcal{L}$ to serve as the seeds; i.e.,

$$S_i = \{s_1, s_2, \cdots, s_M\} \tag{5}$$

where each seed s_j is given by

$$s_j = p_l, \quad \text{where} \quad l = \text{int}\left(\frac{(j-1)\cdot N_{B_r}}{M}\right) + 1, \quad j = 1, \cdots, M, \tag{6}$$

int(·) returns the integer part of its argument, and $M \leq N_{Br}$. In addition, compute a working area by determining the minimum bounding rectangle about B_r and expanding this rectangle by W pixels in all directions (Figure 4c).

(d) Using S_i and the working area (e.g., Figure 4b), apply the 2D live wire automatically to sequentially connect seeds in S_i using the same order (clockwise or counter-clockwise) as for B_r. This gives candidate boundary B_i with cost c_i per (1–2).

(e) If

$$|\bar{c} - c_i| \leq \bar{c}/100 \tag{7}$$

(i.e., the cost has converged), stop the process. Otherwise, replace seeds in S_i with pixels $\in B_i$ that are midway between each successive pair of seeds (s_j, s_{j+1}) in S_i, let $\bar{c} = c_i$, and repeat steps (d)–(e).

(f) Unless a stopping condition is met (e.g., Figure 4d; see below), proceed to the next section by letting $i = i + 1$, $B_r = B_i$, and returning to step (b).

(g) Perform automatic analysis similar to steps (a)–(f) for 2D sections I_i, $i < r$, but proceed in the opposite direction; i.e., let $i = r - 1$, etc.

The final output B consists of all computed 2D contours B_i.

For our ongoing lung-cancer assessment research (and the results in Section 3), we have used 3D regional nodal stations automatically computed by the LNSM to help cue the user interaction tasks of step 1 (Figure 5) [20, 22]. These stations abide by the anatomical definitions of the international standard TNM lung-cancer staging system (T = tumor; N = lymph node; M = distant metastases) [1, 3]. In particular, to select the reference section I_r in step 1(a), the LNSM focuses the user's attention to a 3D subvolume of I corresponding to a particular station, as shown in Figure 5. In addition, after the user decides on I_r, the LNSM automatically provides the requisite rectangular working area for step 1(b). If a facility such as the LNSM is not available, however, interactive graphical functions can easily be devised for selecting I_r and defining working areas [27].

Step 2 involves automatic iterative 3D live-wire analysis. For step 2(b), computation of a new boundary B_i begins with a seed set derived from pixels on the projected B_{i-1}. This is in line with (3), whereby the boundary of B is assumed to change little from one section to the next. Nevertheless, during the automatic iterative live-wire process of steps 2(d–e), if an

early iteration of boundary B_i has inconsistencies, the live wire's optimal search strategy coupled with the iterative adjustment of seed set $\mathcal{S}$ (step 2(e)) generally enables convergence of B_i to a satisfactory contour.

The automatic live wire of step 2(d) performs the bulk of the computation in arriving at a boundary B_i for section I_i. For this operation, we use a slightly modified version of the automatic graph search algorithm given explicitly in the 2D/3D live-wire work of [18]. In particular, the automatic live wire involves the following:

1. For each pair of consecutive seeds (s_j, s_{j+1}), $j = 1, 2,\ldots,M - 1$, in S_i, apply the automatic graph search given by Figure 2 of [18], letting $s = s_j$ and $p = s_{j+1}$.
2. To give the final closed boundary B_i, apply the graph search to seed pair (s_M, s_1).

For step 2(f), automatic processing terminates in a given direction if any of the following stopping conditions are met:

- The cost varies greatly between successive sections:

$$|c_i - c_{i+1}| > c_i/10. \tag{8}$$

  where c_i and c_{i+1} are the final costs $\bar{c}$ for computed contours on I_i and I_{i+1}.

- The boundary of B_i contains too few pixels:

$$N_{B_i} < M \tag{9}$$

  i.e., pixel list $\mathcal{L}$ in (4) consists of fewer than M pixels.

- The region of support of B_i is too small:

$$B_i's \text{ interior consists of fewer pixels than } B_i's \textit{ boundary} \tag{10}$$

- The gray-scale distributions of pixels vary too greatly between successive sections:

$$> \frac{1}{2} \text{of } B_i's \text{ pixels have values outside the range spanned by } B_{i-1}'s \text{ pixels} \tag{11}$$

Condition (8) is motivated by (3), whereby the boundaries between adjacent sections are expected to differ little. Note that, as analysis progresses through I, the number of pixels on list $\mathcal{L}$ in (4) naturally varies from section to section, while the number of seeds M constituting seed set $\mathcal{S}_i$ per (5) in step 2(c) remains the same. Thus, per (6), the spacings of seeds s_j typically vary from section to section. Conditions (9–10) both terminate the process if the support of B becomes too small, as is often expected since a lymph node naturally tends to taper off near its ends. Finally, condition (11) addresses the expected gray-scale consistency of a lymph node between adjacent sections. A large gray-scale distribution change per (11) typically indicates that the target node has vanished and a new region appears.

2.3 Single-Click Live Wire

As demonstrated in Section 3, a significant number of lymph nodes appear as regions that are reasonably well distinguished from their surroundings; i.e., all 3D boundaries of a node

can be defined properly by the automatic live-wire process driven by the gradient-based cost function (1). For such nodes, the single-click live wire is typical effective.

The method, illustrated in Figure 6, is identical to the single-section live wire in all steps except for steps 1(b) and 2(a):

- For step 1(b), the user only needs to select a single cue pixel inside the desired B on I_r (Figure 6a). Automatic processing will later define the reference boundary B_r.
- Step 2(a) is modified as follows. Cued by the selected reference section I_r and cue pixel, an automatic ray search casts rays in M directions from the cue pixel (Figure 6b). The pixels with the largest gradient magnitudes along their respective rays then serve as initial seeds $s_1, s_2, \ldots, s_M$, for $\mathcal{S}_i$ (Figure 6c) for automatic live-wire-based computation of B_r. Processing then proceeds onto section I_i, where $i = r + 1$.

All other processing operations (steps 2(b–g)) are the same as for the single-section live wire.

Figure 6 shows a complete example of applying the single-click live wire to define a station 4 lymph node in a 3D MDCT image.

2.4 Method Comments

Both the single-section and single-click methods are straightforward to learn and use. In our experience, technicians become proficient in applying the methods after a short training session. The single-click method is especially easy to use, as the user need only click any point inside a region. As demonstrated in Section 3, it is often useful to run repeat trials of the single-click method to improve segmentation results; this creates little undue burden given the ease of the single-click method. Furthermore, the results of Section 3 attest to the relative insensitivity of the methods to the selection of the reference section I_r and working areas, as well as the definition of B_r for the single-section method and the selection of the cue pixel for the single-click method.

For all of our tests, we used $M = 8$ seeds for seed set $\mathcal{S}_i$ and $W = 15$ pixels as the working-area expansion amount for step 2(c) of both methods. These choices are in line with expected node sizes and MDCT sampling intervals (Δz, Δy, Δz). Furthermore, these values allow valid node cross-sections to be as small as 9 pixels (3×3 neighborhood) per stopping conditions (9–10), and give very liberally-sized working areas. Also, for cost function (1), we used the weights $w_G = 0.4$, $w_Z = 0.17$, $w_{D1} = 0.33$, and $w_{D2} = 0.1$ — these are the same weights used for more general 3D MDCT chest image efforts of [18].

Our proposed methods improve upon the iterative live wire proposed by Souza *et al.* [17]. The idea behind of the iterative live wire is to progressively converge toward an object boundary using the 2D live-wire method and several initial seeds on or near the boundary. Souza's method, however, adjusts seeds by picking midpoints from segments between pairs of successive seeds used in a previous iteration. The seeds used to construct the final object boundary of current section I_i are then passed on directly as the initial seed set for I_{i+1}. Thus, locations of initial and adjusted seeds for I_{i+1} are roughly correlated to the seed set of I_i. As a result, the initial seed set for I_{i+1} completely relies on the previous section I_i. Segmentation errors, therefore, could accumulate over sections. Furthermore, Souza *et al.* did not describe clear stopping conditions for segmenting 3D objects.

3 RESULTS

This section presents test results evaluating the performance of the proposed methods.

For the first test, a human observer O_1 was given the task of segmenting 50 central-chest lymph nodes present in a series of 5 MDCT scans (10 nodes per scan). The scans were drawn from a database of human 3D MDCT chest scans constructed under a previous IRB-approved protocol [21, 22, 27]. The scans were produced under our University medical center's standard lung-cancer management protocol using either a Siemens Sensation 16, Emotion 16, or Sensation 40 MDCT scanner (Table 1). In addition, as part of the same IRB protocol, a chest radiologist, pulmonologist, and imaging scientist worked in collaboration to locate and painstakingly segment the central-chest lymph nodes in each scan. These segmentations served as ground truth.

The 50 test lymph nodes had typical characteristics, as summarized in Table 2. They appeared in TNM stations 1–2 (highest mediastinal and upper paratracheal), 3 (prevascular/retrotracheal), 4 (lower paratracheal), 5 (subaortic), or 6 (para-aortic); these stations are especially challenging for lymph-node segmentation as they contain an abundance of potentially distracting major vessels and airways [1]. All tests were run on a Dell Precision 650 workstation, using dual Intel Xeon 3.2GHz processors, 3 GB RAM, and Windows XP.

Observer O_1 applied each proposed method over two separate trials, spaced at least one week apart, with the scans and nodes presented to the observer in random order during a trial. For this test and the test to follow, we used the automatically computed 3D regional nodal stations provided by the LNSM to help direct the observer in choosing a reference section I_r for a particular node (Figure 5). The LNSM station also provided the working area for the single-section method, while, for the single-click method, the observer interactively defined the working area on I_r. The observer could repeat the single-click method for a given node if he found the segmentation produced by a particular attempt to be unsatisfactory; a segmentation was judged unsatisfactory if the automatically derived B_r on the reference section appeared incorrect. We permitted up to 3 attempts of the single-click method for a given node. Note that, for any given node, I_r could differ from one trial to the next.

We measured the accuracy, intra-observer reproducibility, processing time, and success rate over all trials. We used the same accuracy and intra-observer reproducibility measures considered in [16, 18]. Accuracy measures how the segmentation $B_{\mathcal{T}}$ ofanode B during trial $\mathcal{T}$ relates to the ground-truth segmentation G and is defined as

$$a(B, G, \mathcal{T}) = 1 - \frac{|B_{\mathcal{T}} \oplus G|}{|B_r| + |G|}, \tag{12}$$

where `⊕' is the exclusive-OR operator and `|·|' denotes the sum of the pixels (volume) constituting its argument. Intra-observer reproducibility measures how segmentations of B compare over separate trials, $\mathcal{T}_1$ and $\mathcal{T}_2$, and is defined as

$$r_{\text{intra}}(B, \mathcal{T}_1, \mathcal{T}_2) = 1 - \frac{|B_{\mathcal{T}_1} \oplus B_{\mathcal{T}_2}|}{|B_{\mathcal{T}_1}| + |B_{\mathcal{T}_2}|}, \tag{13}$$

where $B_{\mathcal{T}_1}$ and $B_{\mathcal{T}_2}$ are the segmentations of B over trials, $\mathcal{T}_1$ and $\mathcal{T}_2$. The measures (12–13) take on values in the range [0, 1], where $a(B, G, \mathcal{T}) = 1$ implies that a segmentation B perfectly matches ground truth G, while $r_{\text{intra}}(B, \mathcal{T}_1, \mathcal{T}_2) = 1$ means that the segmentations done over two trials are identical (but not necessarily accurate!). Processing time includes the time required to perform the interactive operations of step 1 for a node. The processing

time of the single-click method for a given node combines the times of all attempts performed.

Finally, we defined a successful segmentation B_r, as one where $a(B, G, \mathcal{T}) \geq 0.60$. We justify this measure of success as follows. Note that the 50 lymph nodes processed for the test are in fact small relative to image resolution: the long-axis lengths varied from 5.5 mm to 20.1 mm and the volumes varied from 63 mm^3 to 970 mm^3. In particular, the first test node G_1 of scan 21405-64 had long-axis = 10 mm, short axis = 6 mm, and volume = 280 mm^3 — an average-sized node per Table 2. This corresponds to a ground-truth volume $G_1 \approx 9\times9\times15 = 1215$ pixels. If the segmented node B_1 is smaller by just 1 pixel layer in all directions giving a B_1 of size $7\times7\times13 = 637$ pixels, then this would give a maximum possible accuracy equal to

$$a(B_1, G_1, \mathcal{T}) = 1 - \frac{578}{1852} = 0.69$$

per (12). For nodes below average size, this accuracy value would be smaller still if a similarly mild segmentation deviation occurred, and it is an expected outcome for small discretized regions where the boundary constitutes a major part of the volume. Hence, our definition for success is reasonable and, in our experience, admits acceptable segmentations.

Table 3 gives numerical results, while Figure 7 gives 3D renderings of successfully segmented lymph nodes and Figure 8 gives examples of failed segmentations. The results show that both methods effectively segment lymph nodes in challenging circumstances. In fact, for the first time, we report success in computer-based segmentation of central-chest lymph nodes depicted in 3D MDCT images.

The single-section method successfully segmented 90% of the nodes over all trials, while the single-click method achieved an 81% success rate. In addition, both methods exhibited an intra-observer reproducibility near 90% and a mean interaction time ≤ 20 seconds, implying that the methods typically enable efficient production of consistent results over any given trial. As expected, the single-click method, which required a mean of 2 attempts to complete a segmentation (range 1–3 attempts), needed more user interaction time than the single-section method. This is partially offiset by the ease of running the single-click method. Furthermore, these results attest to the robustness of the methods to both the choice of reference section I_r and, in the case of the single-click method, the choice of cue pixel.

Regarding failed segmentations per trial on a given scan (10 nodes per scan trial), 8 of 20 scan trials resulted in 0 failed segmentations (5, single section; 3, single click), 5 of 20 scan trials resulted in 1 failed segmentation (3, single section; 2, single click), 1 of 20 scan trials resulted in 2 failed segmentations (single section), and 6 of 20 scan trials resulted in 3 failed segmentations (1, single section; 5, single click). Neither method failed to segment any node of scan 21405-67. On the other hand, O_1 never successfully segmented 1 node of scan 21405-64, 2 nodes of scan 20349-3-3, and 1 node of scan 20349-3-15 with either method. (The impact of contrast agent was inconclusive in this test.)

Note that the single-click method always failed to segment a node if the single-section method also always failed (Figure 8). This is because the single-click method is only cued by a single point to define the reference boundary B_r; thus, if the reference section I_r has a weak boundary, meaning that the automatically computed B_r is likely to be in error, then the method will fail. Conversely, the single-section method has a complete, and presumably, satisfactory B_r provided interactively by the observer before automatic analysis proceeds.

In an effort to measure inter-observer variability, we next had a second observer O_2 apply the proposed methods to the 20 nodes of scans 20349-15 and 21405-67. O_2 performed this test under the same conditions followed by $O1$ earlier; i.e., two trials on each scan spaced at least one week apart, nodes and scans presented in random order. We computed the accuracy (12), intra-observer reproducibility (13), success rate, and processing time for O_2. In addition, we also computed the inter-observer reproducibility [16, 18]

$$r_{\text{intra}}(B, O_1, O_2) = 1 - \frac{|B_{O_1} \oplus B_{O_2}|}{|B_{O_1}| + |B_{O_2}|}, \tag{14}$$

where B_{O1} and B_{O2} are the segmentations of B by observers, O_1 and O_2, over a given trial, to compare how diffierent observers segment the same nodes.

Table 4 summarizes the results. Both observers exhibited essentially indistinguishable robust performance. In addition, for both methods, the observers produced an inter-observer reproducibility near 90%, attesting to the observer independence in applying the methods.

4 DISCUSSION

In our previous work, we proposed a general 3D live-wire-based segmentation scheme [18]. Both of the new methods proposed now — the single-section and single-click live-wire methods — require significantly less user input than this previously proposed method, while also employing an automatic version of the live wire. The new methods have proven to be especially effective for segmenting central-chest lymph nodes in 3D MDCT scans. This is because lymph nodes, by their anatomical nature, generally appear as isolated soft-tissue structures. Our results indicate a success rate of 90% for the single-section method and an 81% success rate for the single-click method, with inter-observer and intra-observer reproducibilities both near 90%.

Both methods are user friendly and easy to use, with typical interaction times under 20 seconds. Also, the methods are general and could conceivably be applied to other 3D segmentation tasks and image types [27], but we have not verified this conjecture in great detail.

Furthermore, the methods work effectively within our large Lymph Node Station Mapper system, an interactive system for TNM-based nodal station analysis and lymph-node definition [20,22]. Note that the single-section method is slightly more accurate and robust than the single-click method, because the single-section method starts with a complete interactive live-wire-based reference contour B_r, while the single-click method only starts with a pixel known to be contained within B_r. In addition, in our implementation of the single-click method, we have generally required the user to define a more stringently restricted working area on reference section I_r than that used for the single-section method. We believe this is easily modified, however, by improving the ray search for I_r.

The methods can fail for lymph nodes that have blurry or nonexistent boundaries, as can happen in soft-tissue structures depicted in 3D MDCT scans. Significantly, we have applied our methods only to MDCT chest images reconstructed with so-called “soft” reconstruction kernels; i.e., those that exhibit a lower noise level while having blurrier region boundaries than those presented by images reconstructed with “sharp” kernels. We have experimented briefly with the use of edge-preserving filters, such as a 5×5 median filter, as a preprocessing step to sharpen edges and reduce noise, and we have found such filters to be helpful in some cases exhibiting weak boundaries [27,28].

Nevertheless, when preparing for a lung-cancer staging bronchoscopy, it is absolutely imperative that a desired diagnostic lymph node be defined correctly. Hence, to supplement our proposed segmentation methods, the LNSM system contains interactive tools, such as region painting and erasing and the standard live wire, for repairing portions of poorly segmenting nodes.

Note that a typical staging bronchoscopy only involves 1 to 4 candidate nodes; hence, the interaction suggested by our methods places no undue burden on the procedure-planning task. 3D MDCT chest images, however, typically depict upwards of 50 or more lymph nodes, as verified in some of our recent work [21]. In addition, Feuerstein *et al.* have made inroads toward automatic *detection* of all central-chest nodes, but they report only a 14% detection rate [12]. Clearly, fully automatic *segmentation* of chest lymph nodes is a much harder problem and further research would be helpful in this direction. Such research in computer-aided detection and segmentation could facilitate more exhaustive procedure planning and ultimately better disease staging [2, 3].

5 SUMMARY

Central-chest lymph nodes play a vital role in lung-cancer staging. The standard lymph-node staging procedure involves identification of suspect lymph nodes in a chest CT scan followed by bronchoscopic nodal sampling. The three-dimensional (3D) definition of lymph nodes from multidetector computed-tomography (MDCT) images, however, remains an open problem. This is because of the limitations in the MDCT imaging of soft-tissue structures and the complicated phenomena that influence the appearance of a lymph node in an MDCT image. We propose two methods for computer-based segmentation of the central-chest lymph nodes from a 3D MDCT scan. For the first method, referred to as the single-section live wire, the user first applies the standard interactive two-dimensional (2D) live wire to a single 2D section after which automated analysis completes the segmentation process. The second method, referred to as the single-click live wire, is very similar to the single-section method but is almost completely automatic. In ground-truth studies involving human 3D MDCT scans, the single-section method successfully segmented 90% of the designated lymph nodes, while the single-click method gave an 81% success rate. In addition, both methods gave intra-observer and inter-observer reproducibility results near 90%. Furthermore, both methods are efficient in that a typical lymph node can be segmented in under 20 seconds. The methods constitute part of a general computer-based system for the planning and guidance lung-cancer staging procedures.

Acknowledgments

This work was partially supported by grants R01-CA074325, R01-CA151433, and R44-CA091534 from the National Cancer Institute (NCI) of the National Institutes of Health (NIH). The NIH NCI had no involvement in the design of methods and studies in this paper. Pinyo Taeprasartsit served as an operator for the test of Section 3.

References

[1]. Mountain C. Staging classification of lung cancer. A critical evaluation. Clin. Chest Med. Mar.; 2002 23(1):103–121. [PubMed: 11901906]

[2]. Torabi M, Aquino SL, Harisinghani MG. Current concepts in lymph node imaging. J. Nucl. Med. Sept.; 2004 45(9):1509–1518. [PubMed: 15347718]

[3]. Goldstraw P, Crowley J, Chansky K, Giroux DJ, Groome PA, et al. The IASLC lung cancer staging project: proposals for the revision of the TNM stage groupings in the forthcoming (seventh) edition of the TNM classification of malignant tumours. J. Thorac. Oncol. Aug.; 2007 2(8):706–714. [PubMed: 17762336]

[4]. Ueno J, Murase T, Yoneda K, Tsujikawa T, Sakiyama S, Kondoh K. Three-dimensional imaging of thoracic diseases with multi-detector row CT. J. Med. Invest. Aug.; 2004 51(3–4):163–170. [PubMed: 15460902]

[5]. Dalrymple NC, Prasad SR, Freckleton MW, Chintapalli KN. Informatics in radiology (infoRAD): introduction to the language of three-dimensional imaging with multidetector CT. Radiographics. Sep–Oct; 2005 25(5):1409–1428.

[6]. Vining, DJ.; Hemler, PF.; Stelts, DR.; Ahn, DK.; Ge, Y.; Hunt, GW.; Siege, C.; McCorquodale, D.; Honea, DM. Virtual endoscopy: quicker and easier disease evaluation. In: Hoffman, EA., editor. SPIE Medical Imaging 1997: Physiology and Function from Multidimensional Images. Vol. vol. 3033. Feb 23–25. 1997 p. 415-423.

[7]. McAdams HP, Goodman PC, Kussin P. Virtual bronchoscopy for directing transbronchial needle aspiration of hilar and mediastinal lymph nodes: a pilot study. Am. J. Roentgenology. May; 1998 170(5):1361–1364.

[8]. Honea D, Ge Y, Snyder W, Hemler P, Vining D. Lymph node segmentation using active contours. SPIE Medical Imaging. 1997; 3034:265–273.

[9]. Honea D, Snyder W. Three-dimensional active surface approach to lymph node segmentation. SPIE Conf. Image Processing. Feb..1999 3661:1003–1011.

[10]. Yan J, Zhuang T, Zhao B, Schwartz LH. Lymph node segmentation from CT images using fast marching method. Computerized Medical Imaging and Graphics. Jan..2004 28(1)

[11]. Kiraly, AP.; Naidich, DP.; Guendel, L.; Zhang, L.; Novak, CL. Novel method and applications for labeling and identifying lymph nodes. In: Manduca, A.; Hu, CP., editors. SPIE Medical Imaging 2007: Physiology, Function, and Structure from Medical Images. Vol. vol. 6511. 2007. p. 651111-1.p. 651111-9.

[12]. Feuerstein, M.; Deguchi, D.; Kitasaka, T.; Iwano, S.; Imaizumi, K.; Hasegawa, Y.; Suenaga, Y.; Mori, K. Automatic mediastinal lymph node detection in chest CT. In: Karssemeijer, N.; Giger, ML., editors. SPIE Medical Imaging 2009: Computer-Aided Diagnosis. Vol. vol. 7260. 2009. p. 72600V-1.p. 72600V-12.

[13]. Dornheim J, Seim H, Preim B, Hertel I, Strauss G. Segmentation of neck lymph nodes in CT datasets with stable 3D mass-spring models. Acad. Radiol. Nov.; 2007 14(11):1389–1399. [PubMed: 17964462]

[14]. Maleike, D.; Fabel, M.; Tetzlaff, R.; Tengg-Kobligk, HV.; Heimann, T.; Meinzer, H-P.; Wolf, I. Lymph node segmentation on CT image by a shape model guided deformable surface method. In: Reinhardt, JM.; Pluim, JPW., editors. SPIE Medical Imaging 2008: Imaging Processing. Vol. vol. 6914. Mar.. 2008 p. 69141S-1.p. 69141S-8.

[15]. Mortensen EN, Barrett WA. Interactive segmentation with intelligent scissors. Graphical Models and Image Processing. Sept.; 1998 60(5):349–384.

[16]. Falcão AX, Udupa JK, Samarasekera S, Sharma S. User-steered image segmentation paradigms: Live wire and live lane. Graphical Models and Image Processing. July; 1998 60(4):233–260.

[17]. Souza, A.; Grevera, G.; Sun, Y.; Odhner, D.; Suri, N.; Schnall, MD. Iterative live wire and live snake: new user-steered 3D image segmentation paradigms. In: Reinhardt, JM.; Pluim, PW., editors. SPIE Medical Imaging 2006: Image Processing. Vol. vol. 6144. Mar.. 2006 p. 61443N-1.p. 61443N-7.

[18]. Lu K, Higgins WE. Interactive segmentation based on the live wire for 3D CT chest image analysis. Int. J. Computer Assisted Radiol. Surgery. Dec.; 2007 2(3–4):151–167.

[19]. Poon M, Hamarneh G, Abugharbieh R. Efficient interactive 3D livewire segmentation of complex objects with arbitrary topology. Computerized Medical Imaging and Graphics. Dec.; 2008 32(8):639–650. [PubMed: 18722750]

[20]. Lu, K.; Merritt, SA.; Higgins, WE. Extraction and visualization of the central chest lymph-node stations. In: Giger, ML.; Karssemeijer, N., editors. SPIE Medical Imaging 2008: Computer-Aided Diagnosis. Vol. vol. 6915. 2008. p. 69151B-1.p. 69151B-15.

[21]. Lu, K.; Higgins, WE.; Bascom, R.; Mahraj, RPM. Quantitative analysis of the central-chest lymph nodes based on 3D MDCT image data. In: Karssemeijer, N.; Giger, ML., editors. SPIE Medical Imaging 2009: Computer-Aided Diagnosis. Vol. vol. 7260. 2009. p. 72600U-1.p. 72600U-9.

[22]. Lu K, Taeprasartsit P, Bascom R, Mahraj R, Higgins WE. Automatic definition of the central-chest lymph-node stations. Int. J. Computer-Assisted Radiol. Surgery. 2010 under review.

[23]. Gibbs JD, Graham MW, Higgins WE. 3D MDCT-based system for planning peripheral bronchoscopic procedures. Computers in Biology and Medicine. March; 2009 39(3):266–279. [PubMed: 19217089]

[24]. Graham MW, Gibbs JD, Cornish DC, Higgins WE. Robust 3D Airway-Tree Segmentation for Image-Guided Peripheral Bronchoscopy. IEEE Trans. Medical Imaging. April; 2010 29(4):982–997.

[25]. Higgins WE, Gibbs JD, Bascom R, Khare R, Taeprasartsit P. Planning and visualization of accessible, safe bronchoscopy routes: Application to central-chest lymph node biopsy. Am. J. Respir. Crit. Care Medicine. April.2009 179:A6148.

[26]. Cormen, Thomas H.; Leiserson, Charles E.; Rivest, Ronald L.; Stein, Clifford. Introduction to Algorithms. MIT Press; Cambridge, MA: 2001.

[27]. Lu, K. Ph.D. thesis. The Pennsylvania State University, Department of Electrical Engineering; 2010. Multidimensional Image Segmentation and Pulmonary Lymph-Node Analysis.

[28]. Lu, K.; Higgins, WE. Central-chest lymph nodes definition from 3D MDCT image data. In: Karssemeijer, N.; Summers, R., editors. SPIE Medical Imaging 2010: Computer-Aided Diagnosis. Vol. vol. 7624. 2010. p. 76240T-1.p. 76240T-10.

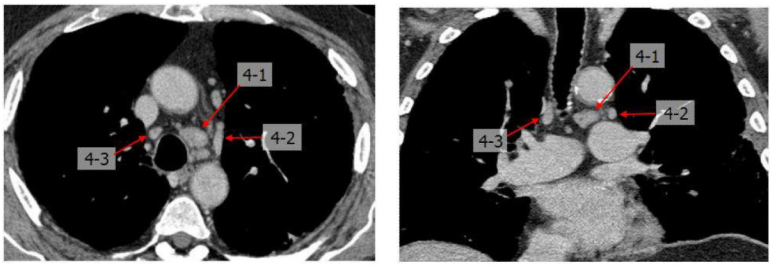

Figure 1.

Examples of central-chest lymph nodes in a 3D MDCT scan. (a) Example transverse-plane (*x*–*y*) section. Three TNM station 4 (lower paratracheal) lymph nodes, labeled 4-1, 4-2, and 4-3, are indicated [1, 3]. (b) Example coronal-plane (*x*–*z*) section depicting the same nodes. These nodes vary greatly in morphological characteristics and are adjacent to surrounding similarly appearing soft-tissue structures, such as major vessels (aorta, azygos vein) and airway walls.

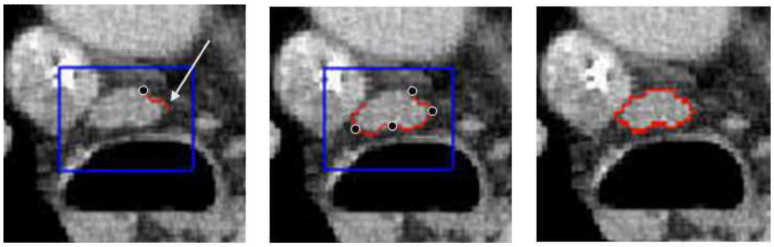

Figure 2.
Example application of the 2D live wire process on a given 2D section I_r. (a) To begin, the first seed s_1 (black dot, added for emphasis) is selected and the mouse cursor is hovered over candidate seed s_2 (indicated by arrow). The background automatic live wire process then computes the optimal path (red contour) between s_1 and s_2 by considering only those pixels within the predefined working (blue box). (b) The user continues this process, with the desired contour gradually being pieced together (four user-selected seeds are highlighted). (c) Final completion of the live-wire process results in a connected contour between the final seed s_6 and initial seed s_1. (Case 20349-3-11-B31, magnified portion of transverse-plane section I_{295}.)

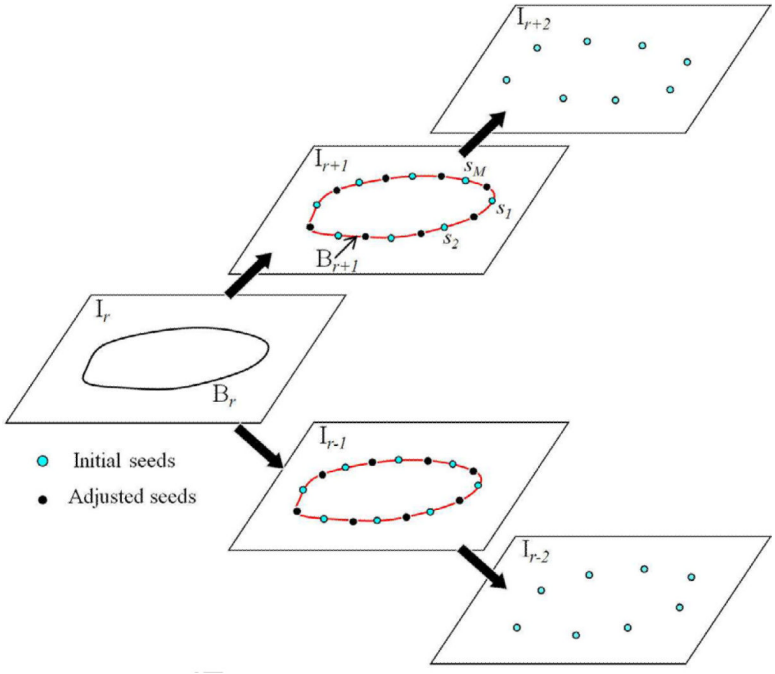

Figure 3.

Schematic view of the single-section live wire. The standard live wire (Figure 2) is first used to define the reference contour B_r on section I_r.B_r is then projected onto 2D section I_{r+1}, and an initial seed seed $S = \{s_1, s_2,\ldots, s_M\}$ is defined based on the pixels constituting B_r. An automatic live-wire process then uses S and a working area to make an initial estimate of lymph node B's 2D boundary B_{r+1}. An adjusted seed set S is then defined based on pixels constituting B_{r+1} and the automatic live wire iterates until convergence or a stopping condition is reached. The process repeats for section I_{r+2} until all sections I_i, $i > r$, have been considered. Automatic processing then occurs for sections I_i, $i < r$.

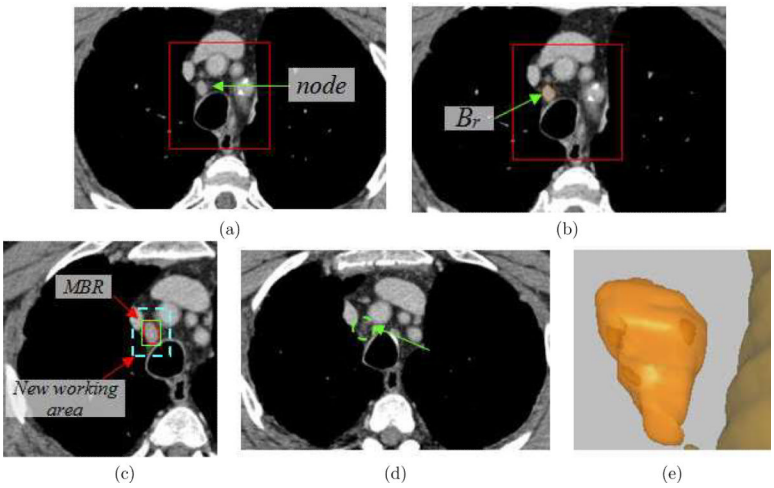

Figure 4.

Use of the single-section live wire to define a station 4 (lower paratracheal) lymph node *B*. (a) Reference section I_r and working area (red box), defined automatically in this case by our LNSM system [20, 22]; target node indicated. (b) Reference boundary B_r defined by the user with the standard 2D live wire on I_r. (c) Automatically computed working area for next section I_{r+1}, defined by finding the minimum bounding rectangle (MBR) about B_r and expanding this box by $W = 15$ pixels in all directions (dotted box). (d) Stopping condition (11) occurs, whereby the pixels in the expected nodal region differ greatly in gray scale than the pixels found for node *B* on the previous section. (e) Final 3D surface-rendered version of node B.

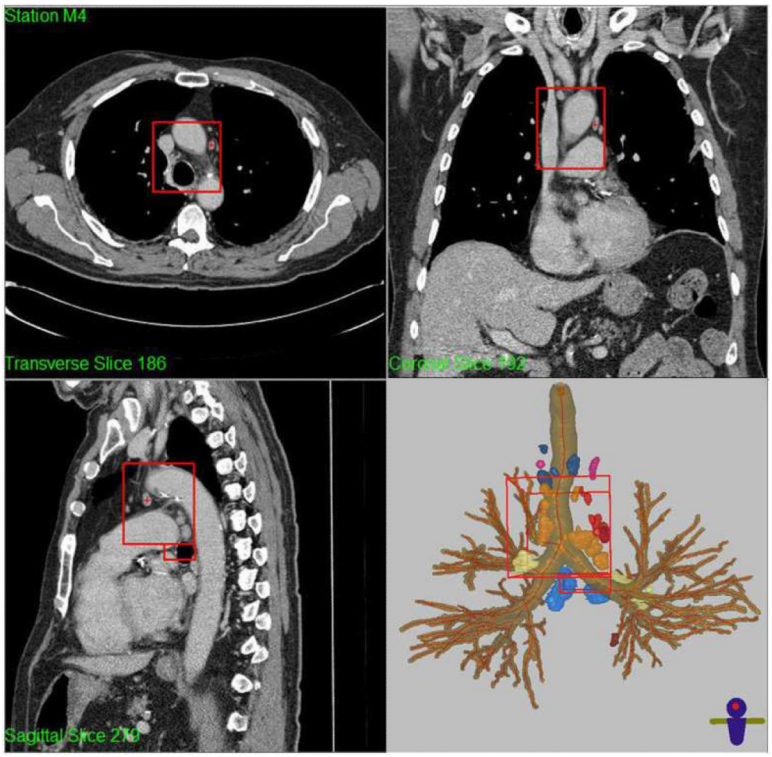

Figure 5.
Example display of the Lymph Node Station Mapper (LNSM) for scan 20349-3-3 [20,22]. The automatically computed 3D volume for TNM regional nodal station 4 is indicated by the red boxes in the various views: upper left - transverse section 186, upper right - coronal section 192, lower left - sagittal section 279, lower right - 3D surface rendering of airway tree with complete 3D station 4. A particular lymph node in the three sectional views is indicated by the red cross. When using the proposed live-wire methods, this station information helps focus attention for finding a reference section I_r and specifies a working area (red boxes on various views). In the figure, the 3D surface rendering depicts all lymph nodes ultimately found for this scan, color coded following the Mountain-based TNM labeling scheme [1].)

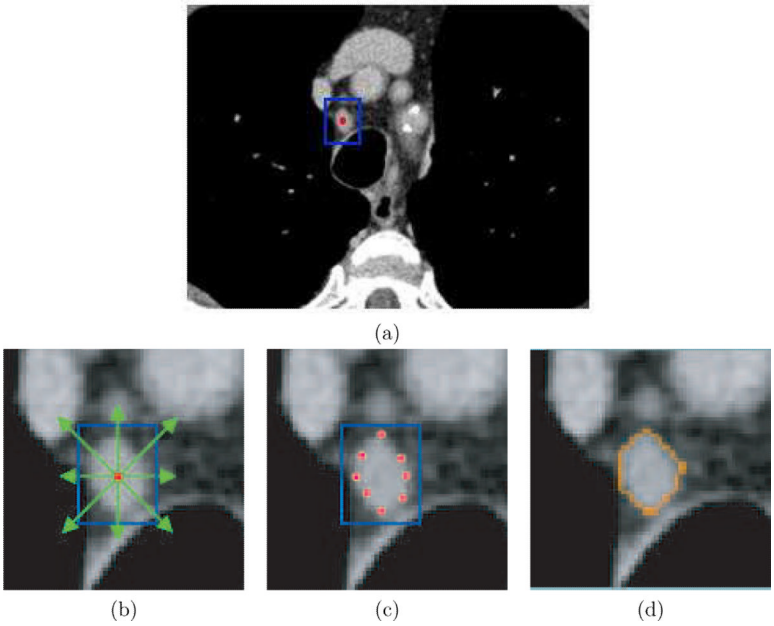

Figure 6.

Illustration of single-click live wire applied to same lymph node considered in Figure 4. (a) On selected reference I_r, the user defines a rectangular working area and selects a cue pixel inside the node. Parts (b–d) then show results of automated analysis (magnified views about target node). Automated analysis (b) casts M rays from cue pixel (M = 8 in this example) and (c) identifies the pixel along each ray having the largest gradient magnitude to serve as seeds s_i, i =1, 2,…,M. (d) Automated live-wire process uses the seed set to define the boundary B_r. The final segmented 3D region is similar to that depicted in Figure 4.

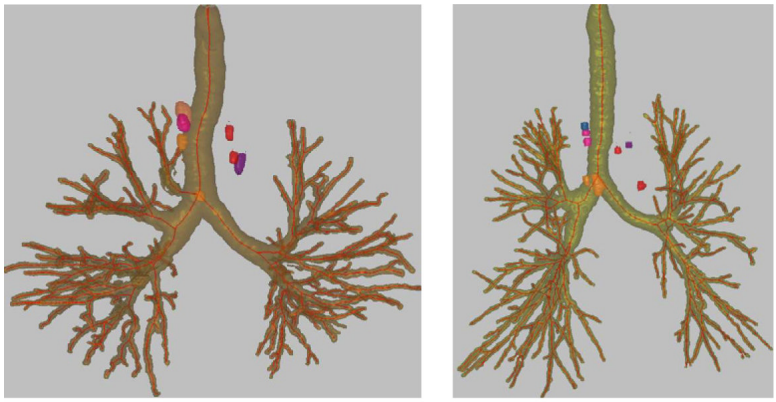

Figure 7.

Lymph nodes successfully segmented by O_1 using both proposed methods. (a) Scan 20349_3_ 3 - 8 nodes. (b) Scan 21405_64_ - 9 nodes. The surface renderings depict the segmented airway tree and centerline (for reference) and the segmented lymph nodes. The colors of the rendered nodes abide by the color scheme of the TNM regional nodal station standard [1]: Blue — stations 1–2 (highest mediastinal and upper paratracheal); Magenta — station 3 (prevascular and retrotracheal); orange — station 4 (lower paratracheal); purple — station 5 (subaortic); red — station 6 (para-aortic).

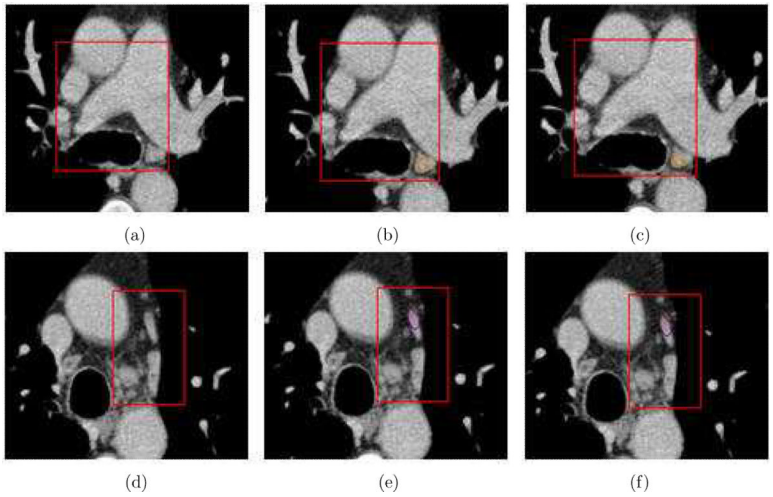

Figure 8.

Two nodes from scan 20349_3_3 where observer O_1 produced failed segmentations. (a) Transverse-plane section I_{231} depicting a station 4 node, which is located in the lower right corner of working area (red box). (b) Successful segmentation of node (a) via the single-section live wire. (c) Failed segmentation of node (a) via the single-click live wire. (d) Transverse-plane section I_{194} depicting station 5 node, which is located in the upper middle region of working area. (b) Failed segmentation of node (d) via the single-section live wire. (c) Failed segmentation of node (d) via the single-click live wire.

Table 1

Characteristics of the 3D human MDCT chest scans used for the tests. All scans had section spacing $\Delta z = 0.5$ mm with (Δx, Δy) representing transverse-plane sampling intervals. Scan 20349-3-27 employed contrast agent, while the others did not.

	Dimensions (mm)		# of sections
Scan	**Δ *x***	**Δ *y***	**in scan**
21405-64	0.64	0.64	702
20349-3-3	0.72	0.72	578
20349-3-15	0.68	0.68	757
20349-3-27	0.67	0.67	752
21405-67	0.69	0.69	716

Table 2

Morphological properties of the 50 lymph nodes considered in the tests. SD = standard deviation.

Property	mean±SD
short-axis length	5.8 ± 1.5 mm
long-axis length	10.5 ± 4.0 mm
volume	256 ± 210 mm^3
number of pixels	1089 ± 861

Table 3

Summary of segmentation results for observer O_1. O_2 applied each of the proposed methods to fifty lymph nodes over two trials. The unit of measure for Accuracy and Intra-Observer Reproducibility is percentage (%). The unit of measure for Processing Time is seconds.

	Single Section		Single Click	
	mean ± SD	**range**	**mean ± SD**	**range**
Accuracy	81± 7	67–97	79± 8	60–93
Intra-Observer Reproducibility	88± 7	74–98	86± 9	61–96
Processing Time	16± 4	7–30	20± 5	7–35
Success Rate	90% (90/100 nodes)		81% (81/100 nodes)	

Table 4

Comparison of the segmentation performance of observers O_1 and O_2. The test involved the 20 lymph nodes of scans 20349-15 and 21405-67 segmented over two trials. The unit of measure for Accuracy, Intra-Observer Reproducibility, and Inter-Observer Reproducibility is percentage (%). The unit of measure for Processing Time is seconds.

	Single Section				Single Click			
	Observer O_1		Observer O_2		Observer O_1		Observer O_2	
	mean ± SD	range	mean ± SD	range	mean ± SD	range	mean ± SD	range
Accuracy	78± 7	61–92	79± 7	62–89	77± 8	63–92	79± 6	67–89
Intra-Observer Reproducibility	88± 7	72–98	88± 9	66–94	77± 8	69–96	79± 8	75–99
Processing Time	17± 4	11–28	17± 4	10–27	19± 4	12–26	23± 4	16–35
Success Rate	95% (38/40 nodes)		95% (38/40 nodes)		92% (37/40 nodes)		90% (36/40 nodes)	
Inter-Observer Reproducibility	88± 8, range: 66–98				86± 8, range: 69–99			